LM-06K035
March 23, 2006

Optical Reflection Spectroscopy of Thick Corrosion Layers on 304 Stainless Steel

R Castelli, P Persans, W Strohmayer and V Parkinson

Optical Reflection Spectroscopy of Thick Corrosion Layers on 304 Stainless Steel

[*]R.A. Castelli[1], P. D. Persans[2], W. Strohmayer[1], V. Parkinson[2]

[1]- Lockheed Martin Corporation, KAPL Inc. P.O. 1072, Schenectady, N.Y. 12301-1072, USA

[2] - Rensselaer Polytechnic Institute, 110 8th Street, Troy, N.Y. 12181, USA

[*]Corresponding author: R. Castelli (518)-395-6735, FAX (518)-395-7298

Keywords: A. Stainless steel; B. in-line diffuse reflection spectroscopy, SEM; C. oxidation, oxide coatings

Abstract: Corrosion resistant structural materials of both iron and nickel based alloys are used in the electric power industry for the construction of the coolant loops of both conventional and nuclear power generating stations. These materials, in the presence of high temperature (e.g. 287° C), high pH (e.g. 10.0 @ 20°C) water with dissolved hydrogen will oxidize and form corrosion films that are double metal oxides (or spinels) of the form AB_2O_4. This work describes optical reflectivity techniques that have been developed to study the growth of these films in situ. The optical technique uses a dual-beam specular reflection spectrometer to measure the spectrum of reflected light in small angle (i.e. < 15°) scatter. The reflection spectra are then calibrated using a set of corrosion coupons with corrosion films that are well known. Results are compared with models based on multilayer reflection and Mie scattering from a particle size distribution. Surface roughness is found to be the dominant cause of reduced reflection as the films grow.

INTRODUCTION

The metal oxide corrosion films formed on iron and nickel based corrosion resistant alloys in high temperature, hydrogenated water have been well studied in isothermal laboratory tests [1, 2]. These films, illustrated in Figures 1 and 2, consist of a relatively thin adherent chromite layer and a larger loosely-adherent ferrite surface layer.

In general, it is believed that the surface ferrite layer is a re-crystallization layer that is formed from divalent metal ions released from the base metal during the oxidation process that then re-deposit on the surface due to hydrothermal crystallization. Figure 2 illustrates that at short exposure times in the hot water, the ferrite crystals (tetrahedral stones) are scattered on the surface on top of the chromite sub-layer that is visible between the crystals. At long exposure times, the ferrite layer crystals grow to in-fill the space between the larger crystals obscuring the view of the chromite sub-layer.

Most of what is known about these corrosion films is derived from the post-test examination of corrosion coupons that are used in closely controlled isothermal laboratory tests. There is however a need to study the effects of a heat flux on the hydrothermal crystallization and dissolution of these metal oxide films. To perform these studies, one will need a measurement technique that can measure and possibly characterize these films as they grow in situ in the presence of a known set of hydrothermal conditions and surface heat flux. Optical reflectance spectroscopy has been demonstrated as a useful in-situ and ex-situ tool for studying growth of thin corrosion films in the case where surface roughness could be neglected [3]. In the present case, surface roughness is not only significant, but it is an important part of the physical description of the system. In this paper we describe the results of optical reflectivity measurements as well as the implications of various approaches to modeling the optical properties.

EXPERIMENTAL DETAILS

Optical reflectivity measurements were carried out using two approaches. Spectroscopic specular measurements were carried out with a dual beam reflection spectrometer. Diffuse angle-dependent scattering was measured using a HeNe laser source and a CCD camera.

The spectrometer system was constructed from off-the-shelf hardware. The source consisted of a 75watt xenon lamp, focused via a parabolic mirror through a 30-slit chopper onto the input slit of a Photon Technology International (PTI) Model 101 Monochromator with a 1200/500 grating. (This equipment is packaged as a single unit PTI Model SID-201 High Intensity Illuminator.) The output from the illuminator is delivered to the measurement system via a PTI Series-380 liquid light guide. The light exits the light guide with a 72° divergence and is collected using a 6.5mm diameter aspheric lens (f#=-2) positioned to focus the beam on the sample coupon approximately 200 mm distant. A 45-degree non-polarizing broadband beam splitter is inserted in the beam prior to the sample in order to provide a reference beam. The split-off reference beam is focused onto a UV enhanced Si photodiode. The remainder (~50%) of the beam is incident on the sample at a 15^{o} incident angle. A 15 mm diameter collection lens is positioned at the center of the specular beam about 200 mm from the coupon. The reflected-beam detector is of the same type as the reference-beam detector. Calibration spectra were measured using an aluminum mirror in order to correct for wavelength dependence of the beam splitter and differences in the detectors. In addition to the specular beam, this system collects light scattered into a cone angle of 5 degrees. The use of a chopper and lock-in detection for both reference and reflected beams filters out signal from other light sources, such as room lights.

To characterize light scattered at larger angles, a HeNe laser (632.8 nm) is used as a source and a collimated beam ~1.5 mm in diameter is incident on the corrosion specimen at ~30^{o} from normal. Scattered and specular light is incident on a fine tracing paper screen placed normal to the specular beam about 30 cm from the specimen and imaged from the opposite side using a Panasonic GP-MF602 CCD Camera. The CCD output signal is recorded using a National Instruments PCI-1407 video capture card. For observation of weak scattered light, the specular beam is blocked prior to the screen. The scattered light is imaged out to about 30^{o} from the specular beam. Measurements are made in a darkened room with a 632.8 nm band pass filter on the detector to reduce background signal.

SPECIMEN PREPARATION

Specimens for the present study are similar to those described in reference [1]. Corrosion specimens of austenitic type 304 stainless steel were exposed at 260^{o}C in a flowing autoclave facility, comprised of a one liter, type 347 stainless steel vessel and fed from stainless steel tanks containing deionized, hydrogen sparged, ammoniated water. Exposure times ranged from 1000 hours to 10,000 hours. One side of each corrosion specimen was polished using diamond grit paste. Specimens were removed from the autoclave for optical studies at room temperature.

STRUCTURAL AND COMPOSITIONAL DESCRIPTION

The effective thickness of the ferrite and chromite layers was determined using x-ray photoelectron spectroscopy with Ar ion milling [2] as well as chemical descaling and weighing. The total mass density from descaling and weighing is given in Table 1 for several specimens. Fitting the net mass density measured for six growth times from 1000 hours to 10,000 hours yields,

$$M_{total} = 1.002\sqrt{t(hrs)} \text{ mg/dm}^2$$
$$M_{Cr} = 0.4203 \times M_{total} \text{ mg/dm}^2 \qquad \text{Eqs. 1a-c}$$
$$M_{Ferrite} = 0.5797 \times M_{total} \text{ mg/dm}^2$$

where M_{Cr} is the mass of the chromite underlayer and $M_{Ferrite}$, is the mass of the ferrite overlayer. In reference [1] it was further shown that the chromite layer comprised about 42% of the total mass of the corrosion film, and the ferrite particles and layer comprised about 58%. The average layer thicknesses T_{Cr} and $T_{Ferrite}$ computed from mass density measurements,

$$T_{Ferrite} = M_{Ferrite} \times 19.3 \text{ nm} \quad \text{and}$$
$$T_{Cr} = M_{Cr} \times 20.1 \text{ nm} \qquad \text{Eqs. 2 a-b}$$

are also shown in Table 1.

Scanning electron-microscope (SEM) photo-micrographs similar to those illustrated in Figure 2 were made of the reference [2] corrosion coupons to measure and characterize

the particle size distributions of ferrite crystals in the surface corrosion film as a function of exposure time to high temperature hydrogenated water. Three different photo-micrograph images were analyzed for each different exposure time using shape recognition algorithms in Image Pro Plus® software. Particle size distributions were obtained from this analysis with a typical population of 7,000-12,000 particles being counted for each distribution.

The raw data (Figure 3) was smoothed and fit with a bi-cubic spline algorithm to create a surface representation (Figure 4) of the changing particle size distribution of ferrite layer crystals as a function of exposure time to high temperature water. The average density ρ of counted ferrite particles decreases with corrosion time as

$$\rho = 5.12 \times \left(t / 1000 \right)^{-0.2563} \text{ particles}/\mu\text{m}^2 \qquad \text{Eq. 3}$$

while the average size increases.

SPECULAR AND DIFFUSE OPTICAL REFLECTIVITY MEASUREMENTS

Near-specular reflectivity spectra

Figure 5 summarizes the dual beam spectra recorded from measurements on each of the specimens in the 15° specular reflection angle geometry. These spectra illustrate that there is sufficient sensitivity in this measurement technique to observe reflection of corrosion films up to greater than 100 mg/dm^2 (10,000 hours). The spectra are smooth, with a broad minimum on the low wavelength end of the spectrum that moves to longer wavelength as corrosion time is increased. The overall magnitude of the reflectivity drops by almost two orders of magnitude between the uncorroded steel surface and the 10,000 hour specimen (M_{tot}= 118 mg/dm^2). This is shown in Figure 6 in which the reflectivity, averaged over 400 to 800 nm, is shown as a function of corrosion film mass. The density of the film not only affects the magnitude of the reflected spectrum, but we

also observe that sometime between the 5,000 and 8,000 hr coupons, the shape of the reflected spectrum above 700nm is also affected.

An image of scattered intensity pattern is shown for the 1000 hour specimen in Figure 7. Most of the scattered intensity is observed in a relatively featureless background, distributed over all angles. Some streaks are observed, which are due to polishing scratches. The widely distributed scattering decreases by about a factor of three between 1000 and 2000 hot hours, and then is relatively independent of hot hours for longer times.

OPTICAL MODELING

The structure of films grown for long times is obviously complex. A full vector field model may be warranted, but has not yet been attempted. The general behavior has been simulated using the simplified model, shown in Figure 8. The cross-section for scattering from each size range of particle is first calculated. The number density of particles in each size range is used to estimate the fraction of the incident beam that scatters from that size. The fractions of the incident beam are then added incoherently. The (wavelength dependent) fraction of the beam that is scattered outside of the acceptance cone of the collection optics is computed first and subtracted from the signal. The remaining beam is incident on the multilayer and treated using standard thin film matrix optics with the assumption that the surface roughness of the rest of the film can be treated as an average microscopically rough interface. This treatment ignores correlated scattering from different particles, but includes coherent thin film effects.

Light will be scattered out of the cone angle of the collection lens by both large and small particles. Particles larger than 0.5 microns are treated using Mie scattering [5, 6]. Specifically, the programs for this work are based on Mie scattering MATLAB programs written by Matzler [7]. Smaller particles are treated by averaging their total mass density into a continuous thin film with roughness equal to a fraction of the film thickness. The probability of scattering from the top layer of large crystals is calculated from direct measurements of the crystal size distribution and density. Because the optical scattering cross section can exceed the physical cross section, care must be taken to avoid over-

counting the scattering from this layer. The total scattering is therefore scaled by estimating the statistical probability that two particles will have overlapping cross sections and subtracting this fraction from the total scattering.

That light which is not scattered out of the collected beam cone by large particles is incident on the next layer. Transmitted light is reflected and scattered from both interfaces of the oxide layer. Standard Fresnel formulas are used to calculate the coefficients of reflection and transmission for the appropriate incident angle. The roughness of the continuous film causes a loss from wide angle scattering given by $TIS = \frac{R_d}{R_o} = 1 - e^{-(4\pi\delta/\lambda)^2}$ [8], where δ is the rms roughness on length scales shorter than the wavelength of the light. Figure roughness, which is due to surface curvature on a length scale much greater than the light wavelength, leads to a wavelength independent decrease in apparent specular reflectivity corresponding to the fraction of the beam that falls outside the collection cone.

The specular reflectivity is thus due to that light which is not scattered and which is then multiply reflected in the thin film structure. This reflectivity is computed using standard thin film multilayer programs [9, 10, 11]. The final specular reflectivity is approximated by $R_{spec} = \left(1 - \sum\left(nSQ_{ext}\right) + \sum nSQ_{fs}\right)R + \sum nSQ_{bs}$, where the sum is over each geometric particle size, with geometric area S; a unit area of surface contains n of these particles; R is the specular reflectivity of the rough film multilayer stack; SQ_{ext} is the extinction coefficient for each particle including all scattering and absorption; SQ_{fs} is the cross section for forward scattering into the cone of the detector; and SQ_{bs} is the cross section for back scattering directly into the cone of the detector.

Although this computational approach can be applied to many thin film and crystallite structures, it is difficult to find a unique structural solution and it is difficult to extract the structural aspects that control the reflectivity behavior. It is therefore informative to compute the effects of multilayer thin film absorption, roughness, and crystal scattering separately to better understand which film properties give rise to the observed optical properties.

Optical constants for stainless steel, chromite, and ferrite

It is important to have realistic optical constants for the various components. The optical constants of various steels have been extensively reported. For the range 400 to 800 nm, the complex index of refraction $\tilde{n} = n + ik$ of 304 steel is given to a good approximation by with n=0.0028λ+0.100 and k=0.0033λ+1.4088, with λ in nm [12]. These constants are consistent with ellipsometric measurements on the substrate steels used in the present study.

The approximate composition and structure of the crystallites and film layers are known from prior work [2], but the optical properties have not previously been reported. The present calculations are made under the assumption that the optical properties of the iron-rich crystallites and top layer are close to those of magnetite (Fe_3O_4) and the optical properties of the lower layer are close to those of ferrous chromite ($FeCr_2O_4$). Values for magnetite are reported in the literature [13] with all reports falling within 10% of the values shown in Figure 9.

The optical constants of $FeCr_2O_4$ have not yet been reported in the open literature. For the present calculations we use optical constants computed from the reflectance spectra of a fine powder [14] using both a dielectric function (oscillator) model and a maximum entropy model for phase retrieval. The reflectance spectrum is essentially the power spectrum of the complex reflectivity:

$$R(\omega) = |r(\omega)|^2 = |\rho(\omega)\exp(i\theta(\omega))|^2$$

The complex refractive index is related to the complex reflectivity by:

$$N(\omega) = n(\omega) + ik(\omega) = \frac{1+\rho(\omega)\exp(i\theta(\omega))}{1-\rho(\omega)\exp(i\theta(\omega))}$$

Therefore, when the reflectance spectrum is known, calculation of the optical constants reduces to the problem of determining the complex reflectivity phase, $\theta(\omega)$. The methods used here are discussed in detail in references [15, 16, 17]. Optical constants deduced using the oscillator model and the maximum entropy model are shown in Figure 10. For the current film reflectivity calculations, the average of these two computed models was used.

The reflectivity of an uncorroded steel coupon is shown in Figure 11. The top theoretical curve corresponds to an ideal surface with no roughness. The measurement (dotted line) is significantly lower than the ideal case. The reduction in reflectivity is most likely due to surface roughness from imperfect polishing. The additional solid curves in Figure 11 correspond to increasing roughness and the best correspondence between specimen and theory is found for a microscopic roughness of 35 nm.

During the earliest stages of corrosion, when the chromite and ferrite layers are less than a few hundred nanometers thick, interference effects may be significant because absorption on one pass through the corrosion layer is low and multiple reflections can occur. For thin films it is expected that roughness effects will also be minimal. Expected interference effects, shown in the model calculations in Figure 12, are consistent with published observations on a similar system [3, 4]. As the corrosion layer thickness increases, a clear reflection minimum forms at short wavelengths and moves upward in wavelength as film thickness increases.

The computed evolution of the ideal specular film thickness is shown for thicker films in Figure 13. As the film thickness is increased, the interference fringe magnitude decreases due to absorption in the corrosion layers and the reflectivity eventually settles into that determined by the optical constants of the top layer, magnetite. Nearly complete damping is found for total thickness of about 750 nm. This would correspond to a corrosion time of about 1500 hours. Therefore under ideal specular film conditions weak fringes might be observed for only the 1000 hour specimen. The theoretical reflectivity of smooth ferrite is basically featureless, with a value of about 0.2. The experimentally observed reflectivity is much lower than that of specular magnetite for thick films and the reflectivity falls off more rapidly for short wavelengths than for long. This suggests that scattering is important.

The computed effect of microscopic roughness alone is shown for the 1000 hour specimen in Figure 14. Backscatter from the top surface into the detector collection cone is included. The computed reflectivity drops sharply when roughness is increased. Decrease at the blue end of the spectrum is greatest. Note that when the computed spectrum matches the experiment at 750 nm, the computed spectrum is much too small at

the blue end of the spectrum. It is therefore clear that roughness alone cannot simulate the observations.

The addition of large surface particles to the model gives rise to scattering loss that is only weakly dependent on wavelength. In Figure 15, the calculated scattered intensity is plotted as a function of angle for 600 nm light incident on a 1000 nm radius particle. Light scattered off of large particles outside of the forward cone and backward cone subtended by the detector optics is lost to the system. For larger particles nearly all of the light is forward scattered. Forward scattered light is incident on the multilayer film and convolved with the multilayer reflectivity. Backscattered light within the cone is captured by the lens and adds directly to the signal. Note that the fraction of backscattered light decreases as wavelength increases. The total scattered intensity is used to scale all scattering calculations and depends on particle size and wavelength. The total scattering cross section is plotted as a function of wavelength for several particle sizes in Figure 16. The total scattering cross section is nearly proportional to geometric area and only weakly dependent on wavelength, with larger interference effects for smaller particles.

The computed signal for corrosion layers corresponding to the samples is shown in Figure 17 along with the experimental data over the range from 450 nm to 750 nm. The simulation includes multilayer reflectivity, microscopic interface and surface roughness of 30 nm, and forward and backscatter from large ferrite particles. Chromite and ferrite mass are taken from Table 1. The overall fraction of the surface covered by large ferrite particles has been permitted to be a fit variable for each of the films, but the size distribution of particles for the simulation is taken from the spline fits in Figure 4. The simulation lines correspond to 25%, 75%, 83%, and 89% coverage for 1000, 2000, 5000, and 8000 hour specimens respectively. Ferrite mass that is not included in large particles is distributed as a rough thin film over the remaining surface.

The fractional area covered by large particles, determined by optical modeling, is well-represented by

$$f = 1 - 219t^{-0.85}. \quad \text{Eq. 4}$$

for t>600 hours. The two measures of large particle coverage are compared in Figure 18.

Integration of the bicubic spline fit to SEM image analysis is shown as the solid line. Fractional coverage from optical fitting is plotted using points. Equation 4 is plotted as a dashed line. The detailed shape of the bicubic integration (solid) line depends on the small particle cut-off of the integration, but the overall shape remains the same. Coverage rises quickly for short corrosion times and then levels off after about 2000 hours.

Based on this fit to the evolution of film thickness and roughness deduced from optical fitting and mass measurements, a model has been developed to predict optical reflectivity based on corrosion time in this system. Inputs to the model include equations 1 and 2 for effective corrosion film mass, the bicubic spline fit to particle size distribution in Figure 4, optical constants shown in Figures 9 and 10, and equation 4 to scale the overall density of large particles.

The final predicted response is plotted in Figure 19a where the reflectivity is simulated in 500 hour steps to long exposure times. Figure 19b illustrates the reflection signal as a function of time at 600 nm and illustrates the presence of interference effects in short exposure times with the power law drop-off in intensity at long times.

CONCLUSIONS

Specular and diffuse reflectivity are clearly useful tools for characterizing both thick and thin corrosion layers on stainless steel. For thin layers, scattering is negligible and interference fringes are evident. It is thus straightforward to determine film thickness and optical constants. For thick corrosion layers, scattering from large ferrite crystallites becomes important and dominates the reflected signal for times greater than a few thousand hours (film thickness > 1000 nm). Backscattering from crystallites leads to a relatively flat reflectivity spectrum. Variation of the aperture for reflected signal collection can elucidate what fraction of the signal is scattered. An optical model that includes thin film interference effects, particle forward and backscattering, and surface roughness has been developed. The growth parameters for a representative set of corrosion films grown in a high temperature, high pH reactor have been used as input to predict the evolution of optical reflectivity and scattering. Computed spectra are in good

agreement with measured spectra and indicate that this type of simulation can be used to deduce film properties for films up to 100 mg/dm^2.

The predictive capability of the model allow the extension of the measurement technique to exposure times (both shorter and longer) not explicitly measured from the calibration coupons.

Future work will address real time spectra measured in situ at high temperature and pressure.

ACKNOWLEDGEMENTS

Donald Buno at KAPL Inc. analyzed the SEM photo-micrographs with Image Pro Plus® that allowed the characterization of particle size distributions.

Several students at Rensselaer contributed to this work. Lukas McMichael, Kennieyanna Padmore, and Dirk Scholvin performed preliminary optical reflectivity measurements. Feiran Huang and Joseph Rapczak contributed to the development of optical models. Herbert Lannon performed diffuse scattering measurements. Shom Ponoth performed ellipsometry measurements and analysis to provide *n* and *k* for the steel substrate.

REFERENCES

[1] Ziemniak, S.E., Hanson, M., "Corrosion behavior of 304 stainless steel in high temperature, hydrogenated water," Corrosion Science 44(2002), pp. 2209-2230.

[2] Ziemniak, S.E., Hanson, M., "Corrosion behavior of NiCrMo Alloy 625 in high temperature, hydrogenated water," Corrosion Science 45(2003), pp. 1595-1618.

[3] Degueldre, C., Fuks, L., Schenker, E., "Preoxidation of stainless steel: a study by diffuse reflection," Applied Surface Science, 134 (1998) pp. 254-262.

[4] Degueldre C, OPrey S, Francioni W, "An in-line diffuse reflection spectroscopy study of the oxidation of stainless steel under boiling water reactor conditions", CORROSION SCIENCE 38 (1996) 1763-1782. (Steel)

[5] Max Born and Emil Wolf, "Principles of Optics", 6th Edition, Cambridge University Press 1980.

[6] C. Bohren and D. Huffman, "Absorption and Scattering of Light by Small Particles" (Wiley, 1998).

[7] C. Mätzler:MATLAB Functions for Mie Scattering and Absorption, Version 2 , IAP Research Report, No. 2002-11, Institut für angewandte Physik, Universität Bern(2002). http://www.iapmw.unibe.ch/publications/pdffiles/199.pdf

[8] J.M. Bennett and L. Mattsson, "Introduction to surface roughness and scattering", OSA, 1989.

[9] M. Klein and Furtak, "Optics" (Wiley, 1986)..

[10] V. M. Pantojas, "Surface and interface roughness in multilayered systems as probed by optical and x-ray scattering". PhD thesis, Rensselaer Polytechnic Institute, 1993.

[11] V. Pantojas, C. Cabral, J. Harper, and P. D. Persans, Mat. Res. Soc. Symp. Proc. **202** 701 (1991)

[12] B. Karlsson and C. G. Ribbing, "Optical constants and spectral selectivity of stainless steel and its oxides", J. Appl. Phys. 53(1982) 6340. (Stainless steel)

[13] A. Schlegel, S. F. Alvarado, and P. Wachter, J. Phys. C:Solid State Physics, 12 (1979) 1157-1164. (Fe3O4)

[14] Reflectance spectra were acquired by Edward A. Cloutis with the NASA RELAB facility at Brown University.

[15] K-E Peiponen, E M Vartiainen, and T Asakura, Dispersion, Complex Analysis and Optical Spectroscopy, Springer Tracts in Modern Physics, Vol. 147, Springer-Verlag, Berlin 1999.

[16] Kai-Erik Peiponen, E M Vartiainen, and T Asakura Dispersion Relations and Phase Retrieval in Optical Spectroscopy, Progress in Optics XXXVII, Elsevier Science B.V., 1997.

[17] Jean-Francois Brun, Domingos de Sousa Meneses, Benoit Rousseau and Patrick Echegut, Dispersion Relations and Phase Retrieval in Infrared Reflection Spectra Analysis, Applied Spectroscopy 55, 774, 2001.

Tables

Table 1 - Mass density and average thickness of corrosion films for various hot water corrosion times.

Time (hours)	Total mass density (mg/dm^2)	Chromite thickness (nm)	Ferrite thickness (nm)
1000	39	294	389
2000	52	416	550
5000	84	658	870
8000	97	832	1101
10,000	118	930	1231

(from least squares fit to total mass data from reference 1)

Figure Captions

Fig. 1 - Cross-sectional view of 304 stainless steel corrosion film after 10,000 hours at 260^{o}C in hot water.

Fig. 2 - Plan view SEM of SS304 corrosion surfaces after 1 kh and 10 kh at 260^{o}C.

Fig. 3 - Particle size distributions for SS 304 corrosion surfaces after 1000, 2000, 5000, and 10,000 hours in hot water.

Fig. 4 - Bi-cubic spline surface fitted to observed particle size distributions on 304-SS corrosion coupons [1] - ($\log_{10}$(frn(dp))

Fig. 5 - Specular reflectivity spectrum of several specimens. Corrosion exposure time corresponding to Table 1 are listed in the figure.

Fig. 6 - Integrated specular reflectivity plotted against mass density.

Fig. 7 - Image of scattered light from 1000 hour specimen. The specimen was illuminated with a narrow HeNe laser beam. Scattered light is projected onto a tracing paper screen and imaged through the screen with a CCD camera. The dark spot in the center is due to the blocking of the central specular spot. The bright streak is due to a macroscopic scratch on the specimen.

Fig. 8 - Simplified structural model for optical modelling calculations. The bottom layer is stainless steel. The second layer is a rough microcrystalline chromite film. The third layer consists of small ferrite crystallites distributed to cover the chromite layer. The top layer consists of ferrite particles larger than 0.5 microns.

Fig. 9 - Complex index of refraction (n, k) for magnetite (Fe_3O_4).

Fig. 10 - Complex index of refraction for chromite ($FeCr_2O_4$) deduced from reflectivity of a fine powder sample.

Fig. 11 - Predicted (solid line) and measured (circles) specular reflectivity for polished stainless steel surfaces. Simulation curves are for various surface roughness parameters from 0 nm (top curve) to 100 nm (bottom curve) in steps of 10 nm. The best simulation of the observation is found assuming an average surface roughness of 35 nm.

Fig. 12 - Computed reflectivity spectrum for ideal thin spinel films on steel. The total corrosion thicknesses are given. Relative thickness of ferrite and chromite films is assumed to be consistent with growth rates for thicker films given above.

Fig. 13 - Computed reflectivity spectrum for ideal spinel films as a function of film thickness from 0 to 1000 nm.

Fig. 14 - Computed reflectivity spectrum for the 1000 hour specimen as a function of top surface roughness from 0 (top line) to 80 nm (bottom line). Experimental reflectivity data are also shown for comparison.

Fig. 15 - Computed scattering intensity for a 1000 nm particle at three wavelengths, plotted as a function of scattering angle.

Fig. 16 -Total scattering cross section plotted against wavelength for particle diameters of 500, 1000, 2000, 4000, 6000, 8000, 10000, 12000, 14000, 16000, 18000, and 20000 nm from bottom to top. The total scattering cross section is nearly proportional to geometric area and only weakly dependent on wavelength.

Fig. 17 - Computed reflectivity signal as a function of wavelength including multilayer specular reflection, rough surface scattering, and particle scattering for varying particle coverage. The top line corresponds to bare steel. Hot hours for corrosion specimens are labeled in the figure. Corrosion layer thicknesses for simulations are computed from independent mass density measurements as described. Fractional surface coverage by large particles has been permitted to vary as a fitting parameter.

Fig. 18 - Fractional surface coverage by large particles deduced from bi-cubic spline fit to distribution from image analysis (solid line) and from optical simulation parameters.

Fig. 19a - Predicted reflection signal plotted against wavelength for time in steps of 500 hours.

Figure 19b - Reflection signal at 600 nm plotted as a function of corrosion time. Early variations are due to interference effects. The reflected intensity drops as a power law in time for long times.

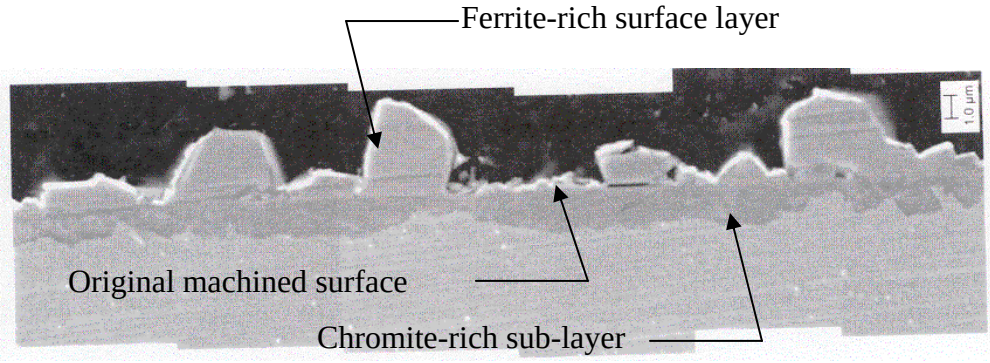

Figure 1 304SS Corrosion Film (117.61 mg/dm^2)[1]

1k hour 304SS coupon (39.25 mg/dm^2)

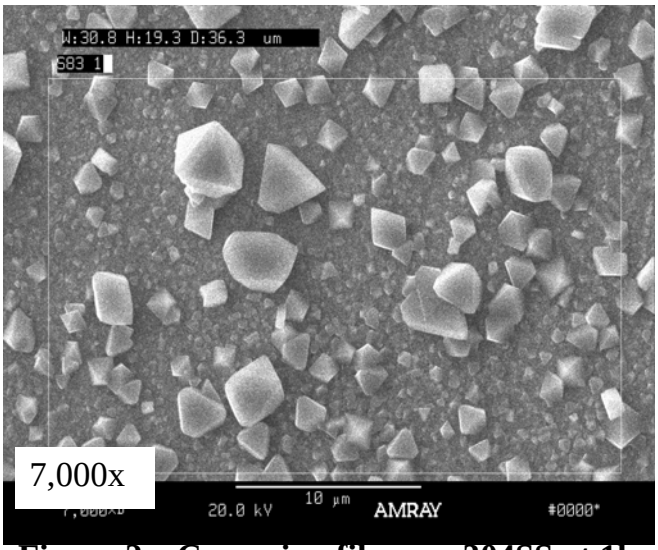

10k hour 304SS coupon (117.61 mg/dm^2)

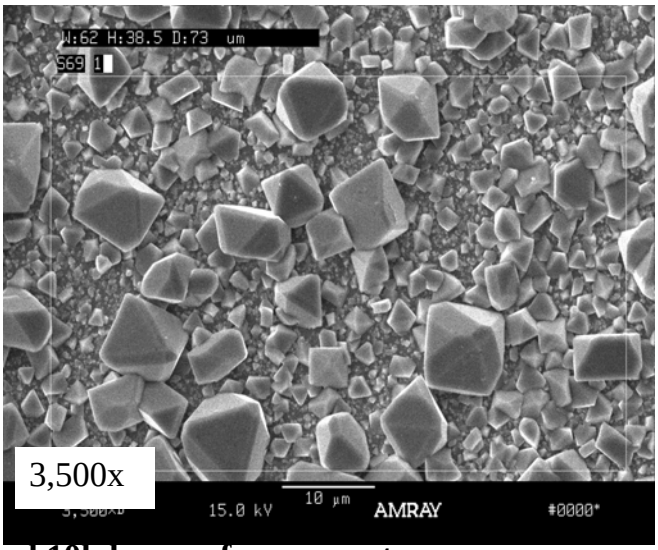

Figure 2 – Corrosion films on 304SS at 1k and 10k hours of exposure to 260°C hydrogenated water[1]

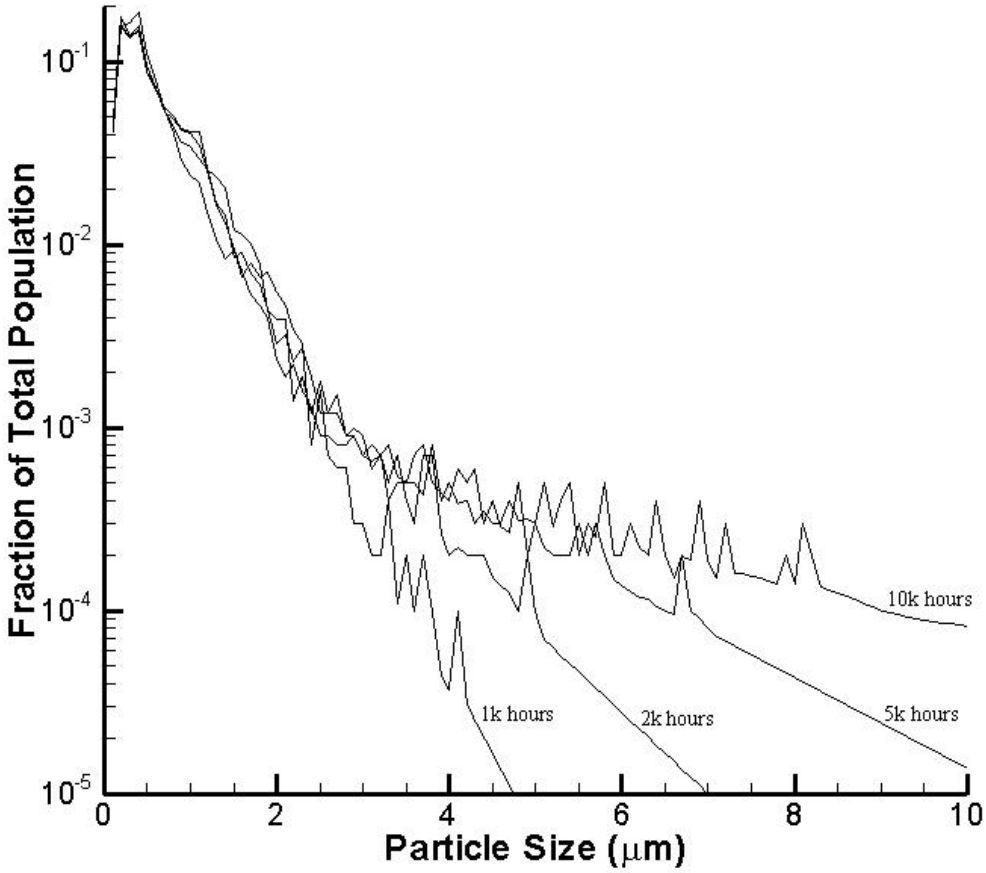

Figure 3 - Particle size distributions for SS 304 corrosion surfaces after 1000, 2000, 5000, and 10,000 hours in hot water.

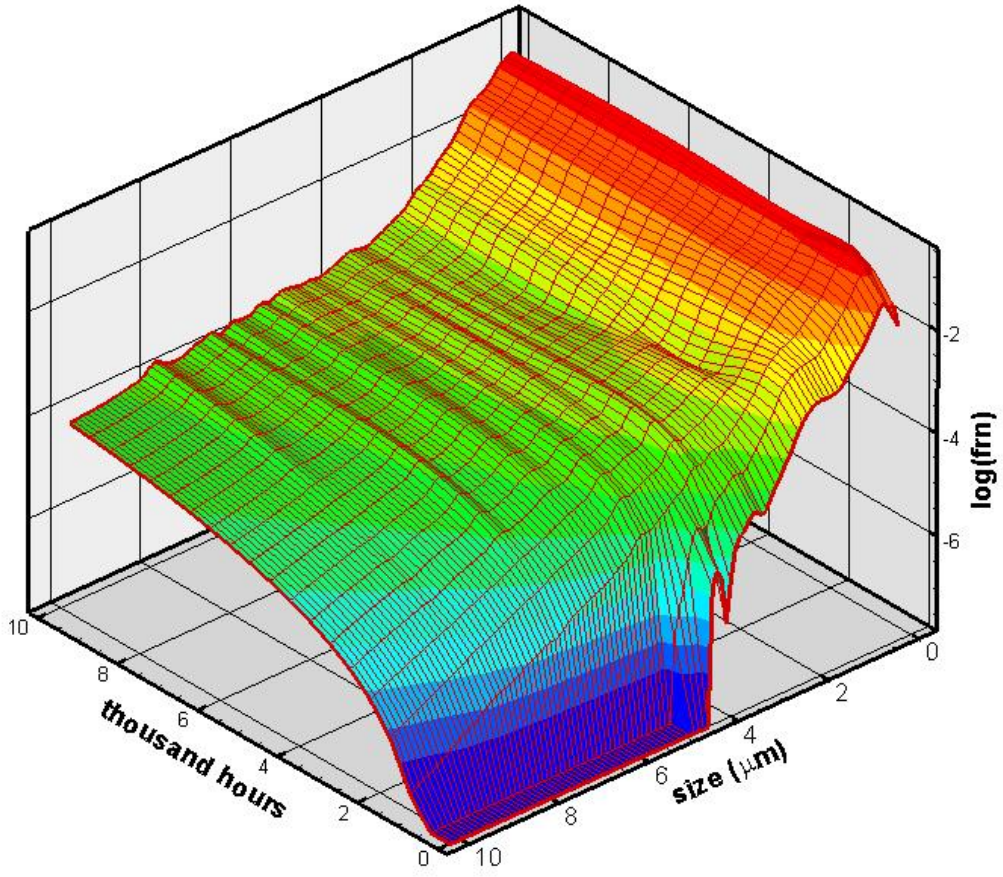

Fig. 4 - Bi-cubic spline surface fitted to observed particle size distributions on 304-SS corrosion coupons [1] - (log(frn(dp))

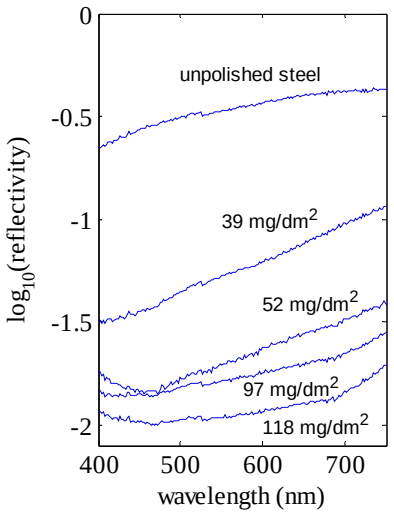

Fig. 5 - Optical reflectivity at room temperature in air, measured as discussed in the text.

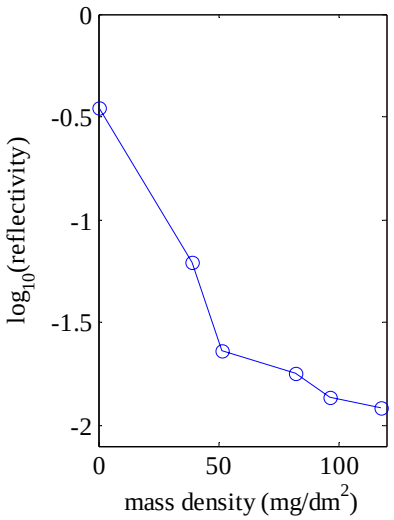

Fig. 6 - Specular reflectivity summed over all wavelengths from 400-800 nm, plotted against specimen corrosion time in hours.

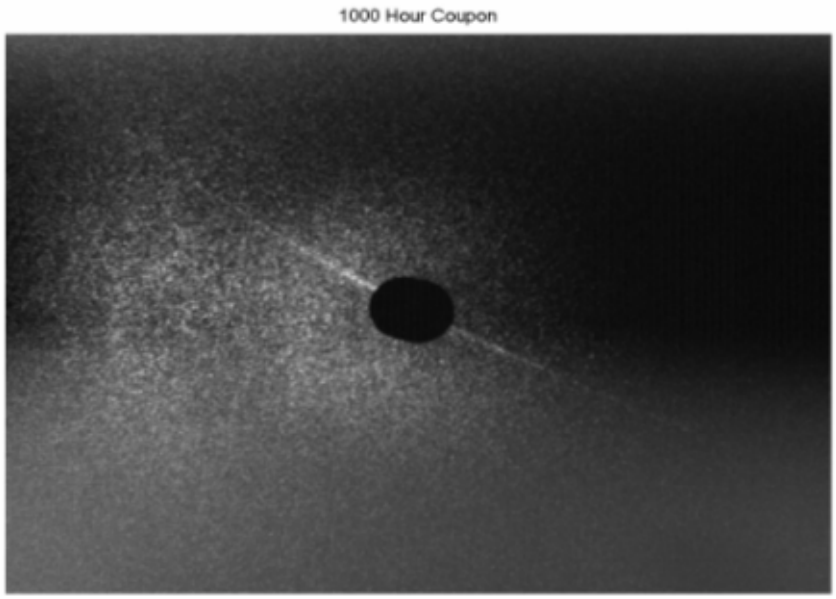

Fig. 7 - Scattered intensity as a function of position on a screen. Illumination source was a HeNe laser. The dark spot at the center is due to blocking of the specular beam.

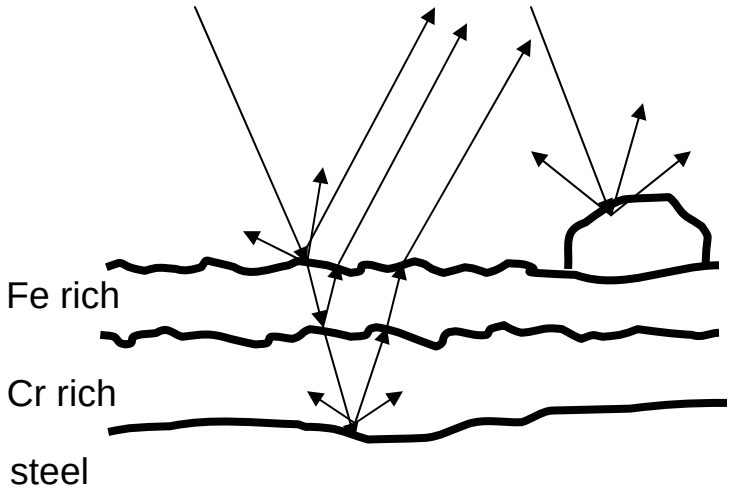

Fig. 8. - Structural model for optical modelling. The inner layer is a chromium rich spinel and the outer layer and large particles are ferrite-rich spinel. The average thickness of the layers evolves with time as discussed in the text.

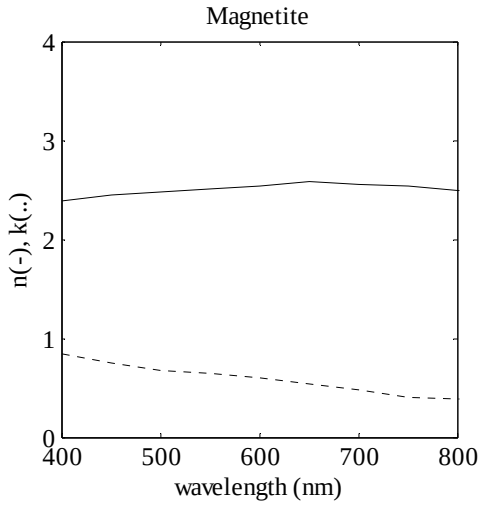

Figure 9 - Real (n) and imaginary (k) index components for Fe_3O_4 [13].

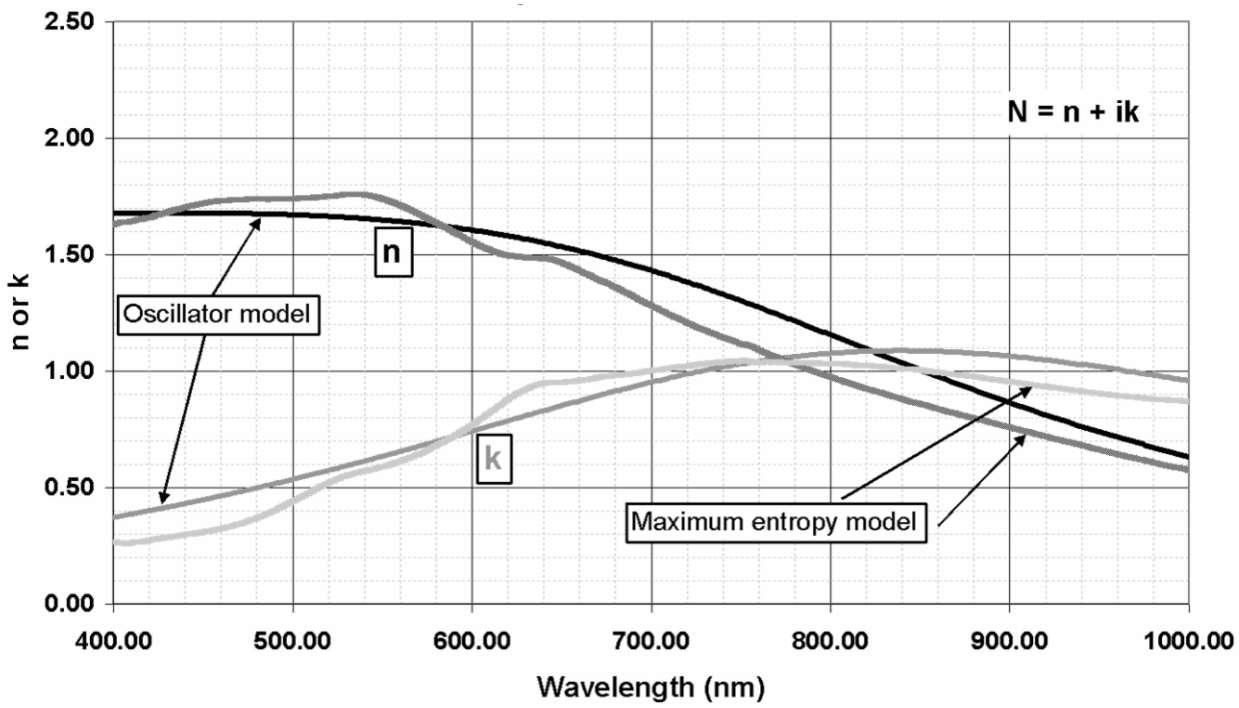

Fig. 10 – Optical Constants for $FeCr_2O_4$ computed in the present work from the diffuse reflection spectrum of a fine powder.

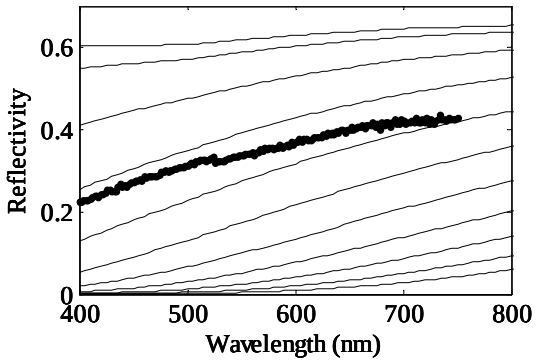

Fig. 11 - Predicted (solid line) and measured (circles) specular reflectivity for polished stainless steel surfaces. Simulation curves are for various surface roughness parameters from 0 nm (top curve) to 100 nm (bottom curve) in steps of 10 nm. The best simulation of the observation is found assuming an average surface roughness of 35 nm.

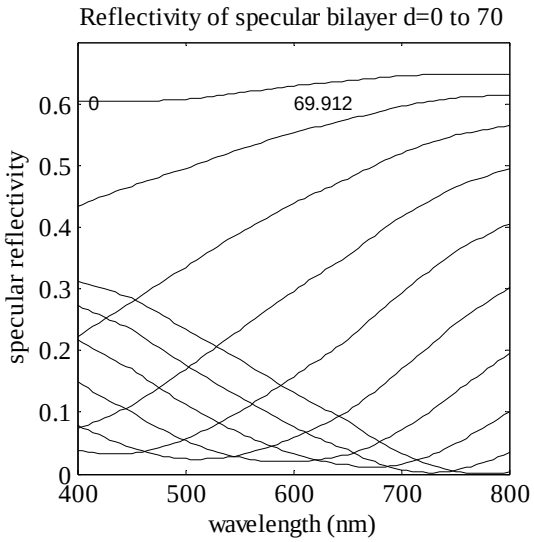

Fig. 12 - Computed reflection spectra for a thin ferrite/chromite bilayer on steel. The total bilayer thickness varies from 0 to 70 nm in steps of 7 nm.

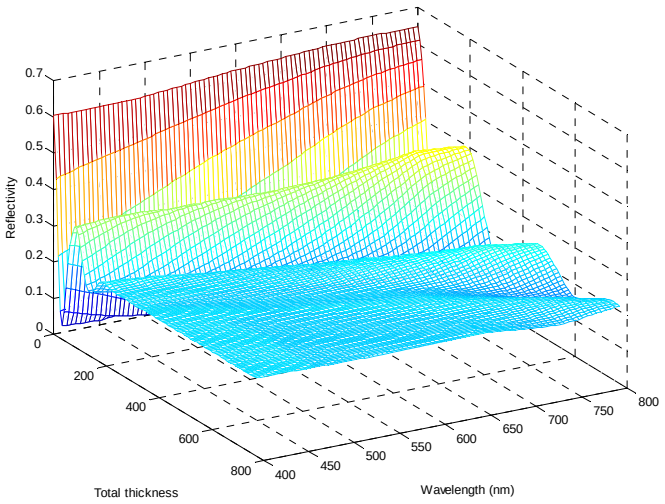

Fig. 13 - Computed reflectivity of a ferrite/chromite bilayer on steel, plotted as a function of total film thickness and wavelength.

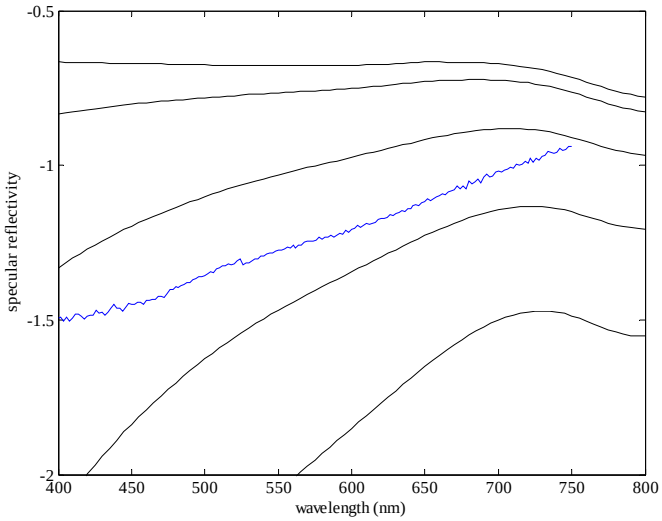

Fig. 14 - Computed (smooth lines) and experimental reflectivity data (jagged line) for the 1000 hour specimen. Roughness is varied from 0 nm (top line) to 80 nm (bottom line) in steps of 20 nm.

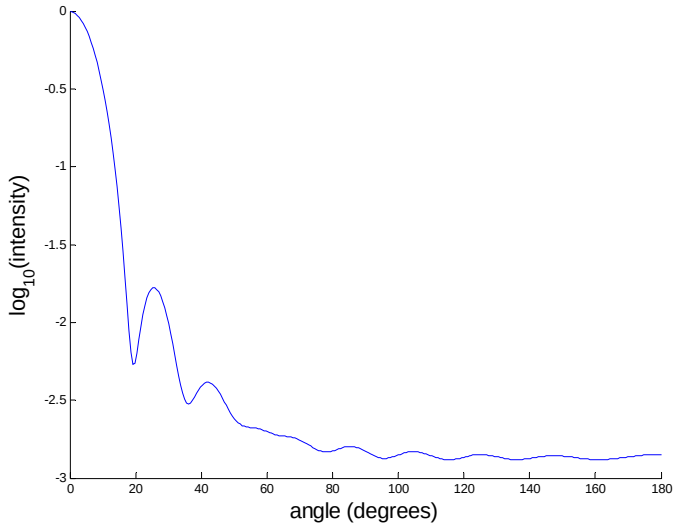

Fig. 15 - Computed scattering from a 1000 nm radius magnetite particle plotted against scattering angle for incident wavelength of 600 nm. Scattered intensity is normalized to the forward signal.

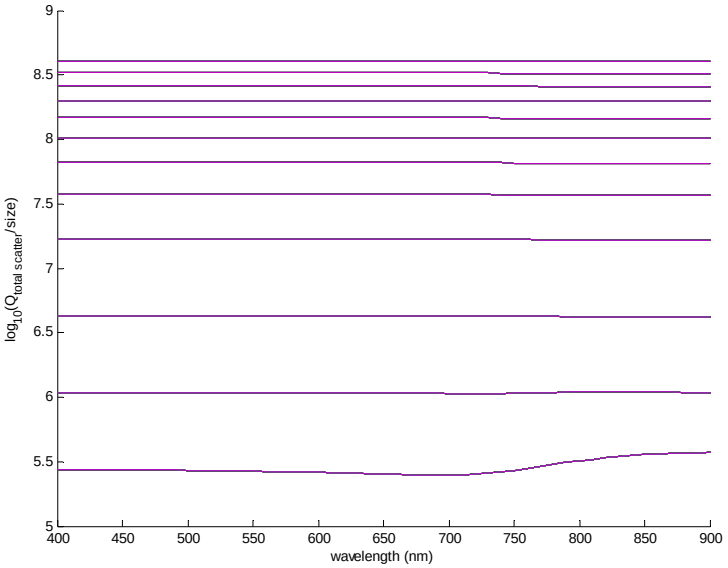

Fig. 16 -Total scattering cross section plotted against wavelength for particle diameters of 500, 1000, 2000, 4000, 6000, 8000, 10000, 12000, 14000, 16000, 18000, and 20000 nm from bottom to top. The total scattering cross section is nearly proportional to geometric area and only weakly dependent on wavelength.

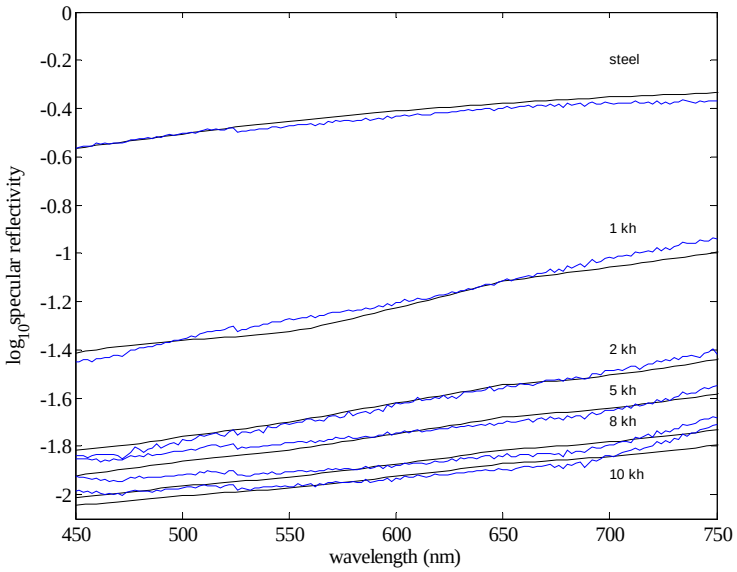

Fig. 17 - Computed and experimental reflection signal plotted against wavelength. The top line corresponds to bare steel. Hot hours for corrosion specimens are labeled in the figure. Corrosion layer thicknesses for simulations are computed from independent mass density measurements as described. Fractional surface coverage by large particles has been permitted to vary as a fitting parameter.

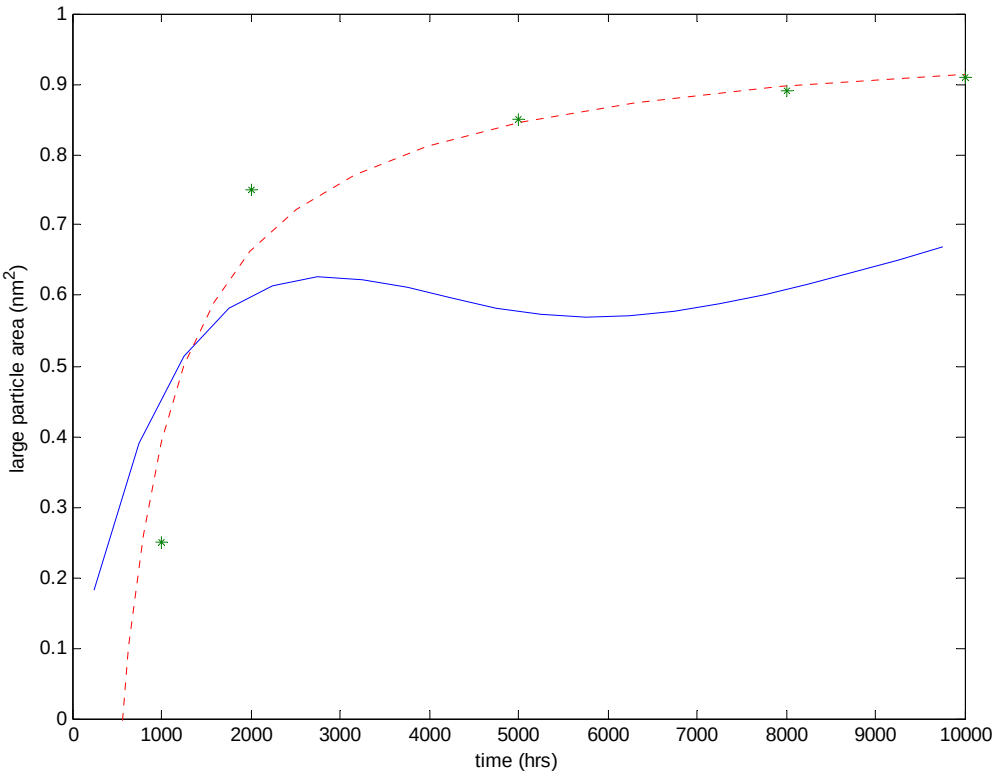

Fig. 18 - Fractional surface coverage by large particles deduced from bi-cubic spline fit to distribution from image analysis (solid line) and from optical simulation parameters.

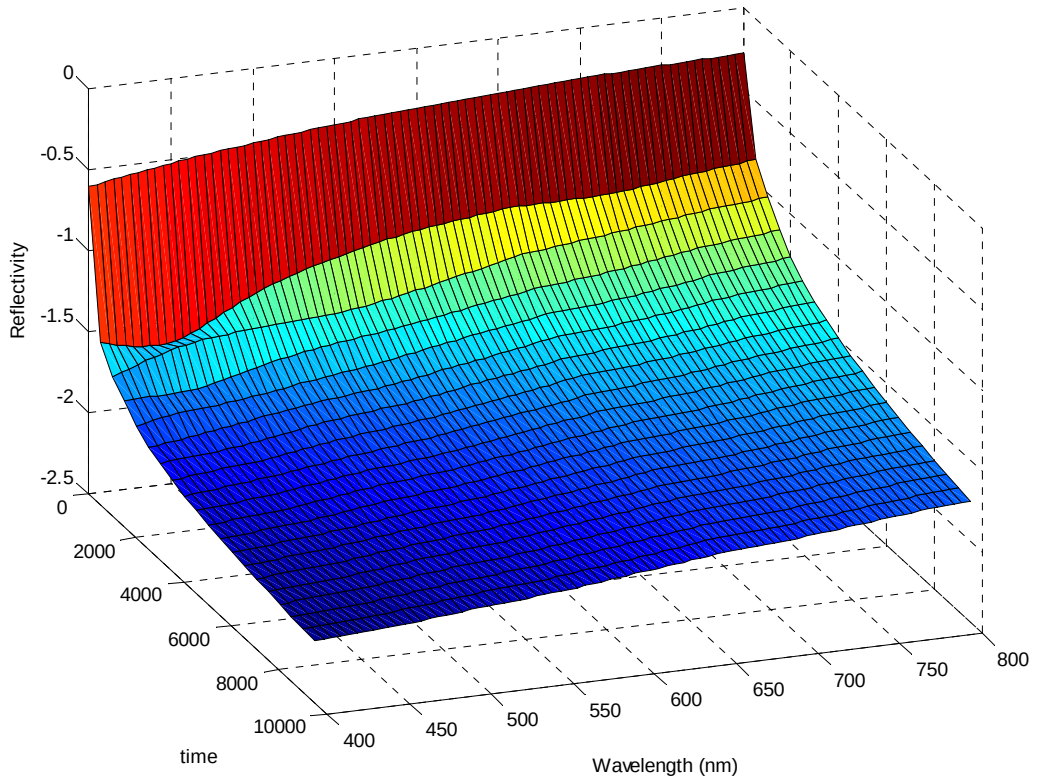

Fig. 19a - Predicted reflection signal plotted against wavelength for time in steps of 500 hours.

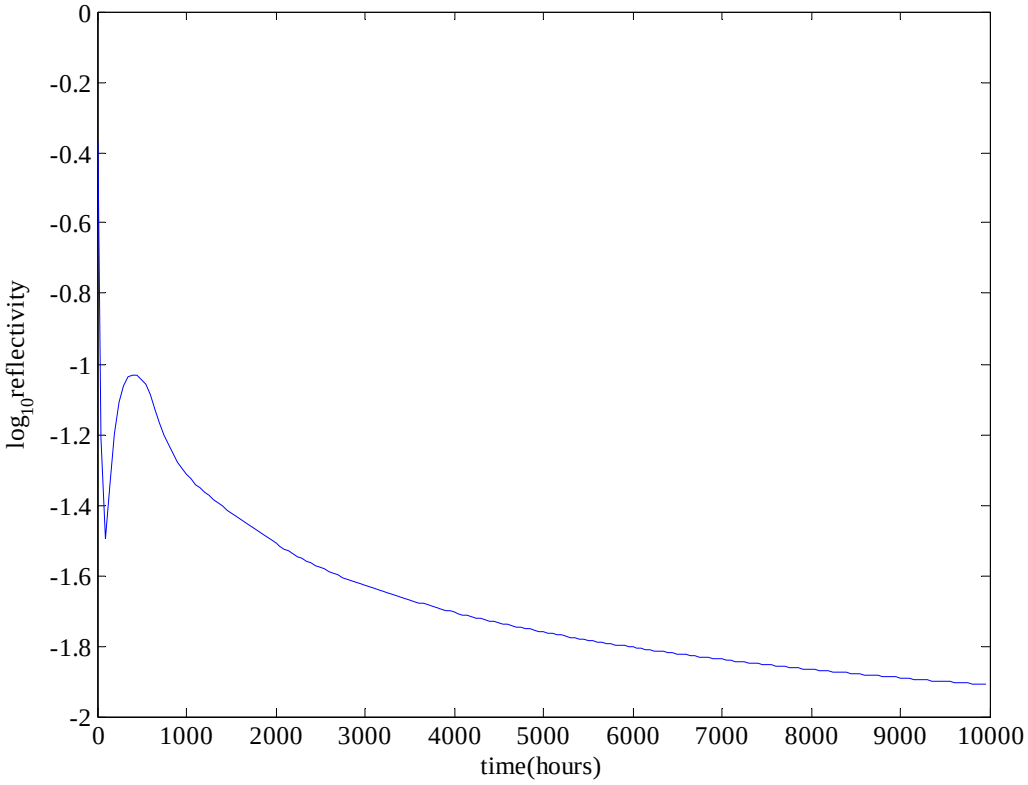

Fig. 19b) - Reflection signal at 600 nm plotted as a function of corrosion time. Early variations are due to interference effects. The reflected intensity drops as a power law in time for long times.

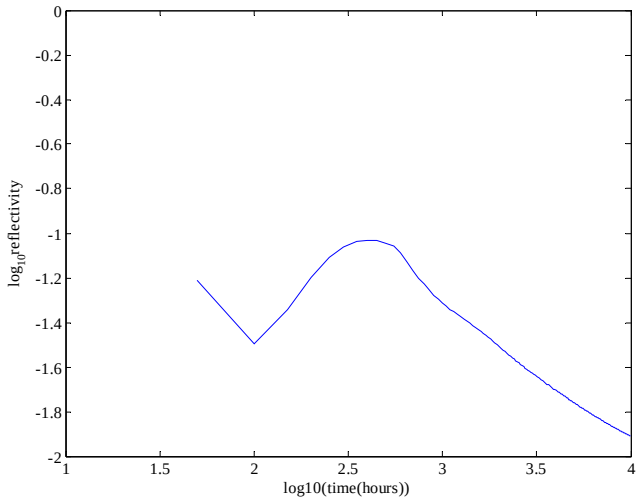
0
-0.2
-0.4
-0.6
-0.8
-1
-1.2
-1.4
-1.6
-1.8
-2
log10reflectivity
1
1.5
2
2.5
3
3.5
4
log10(time(hours))

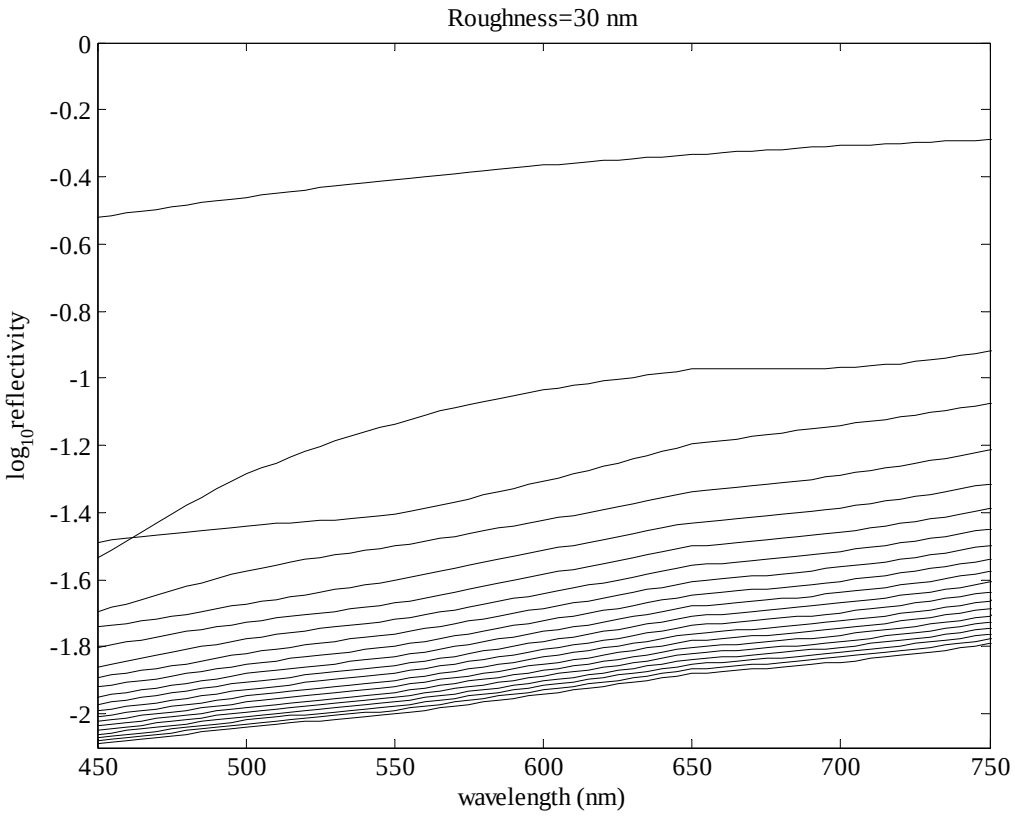

same plot as 19 in 2 d version